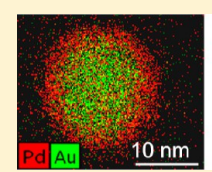


From Core—Shell to Alloys: The Preparation and Characterization of Solution-Synthesized AuPd Nanoparticle Catalysts

Adria R. Wilson,[†] Keyi Sun,[‡] Miaofang Chi,[§] Ryan M. White,^{||} James M. LeBeau,^{||} H. Henry Lamb,*,[‡] and Benjamin J. Wiley*,†

Supporting Information

ABSTRACT: This article describes the solution-phase synthesis of 4 nm gold nanoparticles with 0.7 atom-thick, 1.9 atom-thick, and 3.8 atom-thick layers of Pd on their surfaces. These well-defined core-shell nanoparticles were deposited on a silica support, calcined, and reduced at 300 °C to create alloyed nanoparticles containing 10.9, 20.2, and 28.5% Pd (w/w). Monometallic Pd nanoparticles sintered during calcination at 300 °C, but no sintering was observed for AuPd nanoparticles. Diffuse reflectance infrared Fourier transform (DRIFT) spectra of adsorbed CO suggests that Au donates d





electron density to Pd in the core-shell and alloy structures and confirms the presence of Au and Pd atoms on the surface of the nanoparticles after calcination and reduction. The properties of the AuPd alloy catalysts were tested in the vapor-phase conversion of α -limonene to p-cymene. AuPd nanoparticles containing 20% or more Pd per particle produced p-cymene yields greater than 80%, equivalent to conventional Pd catalysts prepared by incipient wetness and ion exchange methods. Very low yields of p-cymene were obtained from dehydrogenation of p-menthane under equivalent conditions, suggesting that the production of p-cymene from α -limonene proceeds through terpinene intermediates.

INTRODUCTION

Alloy catalysts can offer greater reaction-specific catalyst tunability, lower cost, and higher performance than their monometallic counterparts. The study of alloy catalysts offer scientists the opportunity to better understand how the interplay between different metals in the nanoregime affects the outcome of heterogeneously catalyzed chemical reactions. AuPd catalysts have been of particular interest not only because of the wide range of reactions in which they can be used but also because of their relative simplicity. Au and Pd are soluble at all compositions, so that the effects of different phases need not be considered.^{2,3} In many reactions, Au is catalytically inert, so any catalytic activity can be ascribed to Pd. To date, a variety of mechanisms have been proposed for the greater catalytic activity and selectivity of AuPd compared to Pd alone.4-Enache and co-workers found that AuPd/TiO2 is twice as productive as Pd for benzyl alcohol conversion to benzaldehyde and proposed that Au is an electronic promoter of Pd. Vinyl acetate monomer production is enhanced 13-fold over 1:4 AuPd/SiO₂ nanoparticles relative to Pd/SiO₂, and this has been attributed to changes in the electronic and geometric properties of Pd upon alloying with Au.⁸ Studies of vinyl acetate formation rates over submonolayers of Pd on single-crystal gold surfaces suggest isolated pairs of Pd on Au(100) enhance binding of acetate with ethylene, and suppress the formation of reaction byproducts.⁸ An AuPd/SiO₂ catalyst with 0.2 monolayer coverage of Pd hydrogenated propene with 12 times the activity of Pd alone; the authors proposed Au breaks up 3-fold surface sites of Pd, and thereby increases the formation of highly reactive propylene relative to less reactive propylidene. Similar enhancements of AuPd relative to Pd are observed in many other reactions. These examples suggest that the specific way in which Au enhances Pd activity varies depending on the reaction being catalyzed and that a clearer, more general depiction of the mechanisms by which AuPd exhibits relatively greater activity, selectivity, and stability will begin to emerge only after examining its properties in a wide variety of reactions.

The conventional wet-impregnation and coprecipitation methods used in many of the studies cited above result in a catalyst structure consisting of nanoparticles with a range of sizes and compositions. The ambiguous structures of these catalysts make it difficult to map out their structure-dependent properties. Various authors have developed colloidal methods in an attempt to produce well-defined nanoparticle cata-

Received: April 26, 2013 Revised: July 8, 2013 Published: July 9, 2013

Department of Chemistry, Duke University, 124 Science Drive, Box 90354, Durham, North Carolina 27708, United States

[‡]Department of Chemical and Biomolecular Engineering, North Carolina State University, Box 7905, Raleigh, North Carolina 27695, United States

[§]Microscopy Group, Oak Ridge National Laboratory, 1 Bethel Valley Road, Building 4515, MS 6064 Oak Ridge, Tennessee 37831,

 $^{^{\}parallel}$ Department of Materials Science & Engineering, North Carolina State University, Box 7907, Raleigh, North Carolina 27695, United

lysts.^{2,13,17-19} However, previous efforts to produce polymerfree (calcined), oxide-supported AuPd nanoparticles in a catalytically relevant size range (≤5 nm in diameter) have resulted in nanoparticles with an unknown range of compositions and with standard deviations in particle size on the order of the nanoparticle diameter.^{17,20} Thus, despite the numerous articles focused on AuPd, there remains a need for methods that produce model AuPd catalysts consisting of nanoparticles with a very narrow range of sizes and compositions.

We have used solution-phase synthesis to produce a series of polyvinylpyrrolidone (PVP)-stabilized AuPd core-shell nanoparticles that have palladium shell thicknesses of 0.7 ± 0.2 , 1.9 \pm 0.3, and 3.8 \pm 0.8 atomic monolayers of Pd as calculated from high-angle annular dark field scanning transmission electron microscopy (HAADF-STEM) images. The coreshell nanoparticles were deposited on a silica support and transformed into alloyed nanoparticles consisting of 10.9 ± 2.3 , 20.2 ± 4.3 , and $28.5 \pm 6.0\%$ Pd per nanoparticle, respectively, through calcination and reduction at 300 °C. An advantage of using a core-shell precursor to produce alloyed nanoparticles is that it facilitates the determination of the per-particle Pd content by measuring changes in shell thickness via standard bright-field TEM and HAADF-STEM. This study represents the first attempt to characterize the structure and properties of AuPd catalysts made by heating and alloying core-shell AuPd nanoparticles.

We examined the catalytic properties of these AuPd alloy catalysts, along with conventionally prepared Au/SiO₂ and Pd/ SiO₂ catalysts, in the conversion of limonene to p-cymene. Currently, p-cymene is produced from petroleum for use in resins, fragrances, pesticides, and solvents.21-24 A more environmentally friendly process is to produce cymene from α -limonene, an abundant waste product of the citrus juice industry.²² Both Pd and Au have been tested as monometallic catalysts for the conversion of limonene to p-cymene. Pd catalyzes the conversion of limonene to p-cymene with high selectivity, but Au exhibits almost no activity.²² A proposed mechanism for the production of p-cymene over Pd/SiO₂ is through the dehydrogenation of *p*-menthane. ^{22,25} The performance of supported AuPd catalysts for limonene conversion has not been tested. We have chosen to study the activity of supported AuPd nanoparticles in limonene conversion not only to explore their potential as catalysts for the production of pcymene from waste but also to gain additional insights into the Pd-catalyzed conversion mechanism using these well-defined alloy catalysts.

EXPERIMENTAL METHODS

Chemicals. Gold(III) chloride trihydrate (520918), sodium citrate tribasic dihydrate (S4641), sodium tetrachloropalladate-(II) (205818), hydroquinone (H9003), polyvinylpyrrolidone MW = 55,000 (856568, PVP55), and polyvinylpyrrolidone MW = 29,000 (234257, PVP29) were purchased from Sigma-Aldrich. Hydrochloric acid (UN1789) and p-menthane (320-53122) were purchased from Fisher Scientific. Limonene (10162783), p-cymene (A0300974), acetone (BDH1101-4LP), ethanol (UN1170), terpinolene (TCT0817-025 ML), α -terpinene (TCM0318-025 ML) were purchased from VWR. Palladium-(II) nitrate hydrate (22403000) and palladium tetrammine dinitrate (19843400) were purchased from Strem Chemical, and the silica used for all of the catalysts was Aerosil 300 from

Degussa (specific surface area = $300 \text{ m}^2/\text{g}$). All chemicals were used without further purification.

Synthesis of Au Nanoparticles. Stirring rapidly, 980 μ L of 1% (w/w) HAuCl₄(aq) solution was added to 100 mL of DI H₂O in a round-bottom flask. To this, 740 μ L of 1% (w/v) sodium citrate and 3 mL of 0.1 M NaBH₄(aq) were added in immediate succession. The NaBH₄(aq) solution was chilled to 0 °C in an ice bath prior to use. Upon the addition of NaBH₄(aq), the solution immediately turned pink—orange in color, indicating nanoparticle formation. The solution was left to sit for 1 h before use, during which time it turned bright red.

Synthesis of 0.7, 1.9, and 3.8 ML Pd@Au Nanoparticles. Making AuPd core-shell particles with different shell thicknesses required varying the amounts of reducing agent and Pd introduced to the Au seed particle solution. In each case, the Au seed solution was stirred at 450 rpm and room temperature, and the reactions were run for 3 h after the initial addition of Pd. For 0.7 Pd@Au, 2 mL of 1% (w/v) hydroquinone was added to 100 mL of Au seed solution, and 2.5 mL of 2 mM aqueous disodium tetrachloropalladate (Na₂PdCl₄(aq)) was infused into the solution at 67 μ L/min. The 1.9 Pd@Au particles were synthesized in 50 mL batches so that the Na₂PdCl₄ solution could be completely infused at the same rate (67 μ L/min) within the three-hour reaction time. In this case, 1 mL of 1% hydroquinone was added followed by the infusion of 9.65 mL of 2 mM Na₂PdCl₄(aq) at 67 μ L/min. To make the 3.8 Pd@Au particles, 4 mL of 1% hydroquinone and 2 mL of 20 mM Na₂PdCl₄(aq) were added, the Pd solution being introduced all at once. At the end of the reaction, 2 mL of 1% (w/v) HCl(aq) was pipetted into 100 mL of the 0.7 and 1.9 Pd@Au solutions, or 4 mL of 1% (w/v) HCl (aq) into 100 mL of the 3.8 Pd@Au solution, to stop the reaction, followed by 4 mL of 1% (w/v) PVP55 aqueous solution to stabilize the particles.

Synthesis of Pd Nanoparticles. PVP-stabilized Pd nanoparticles were synthesized via a method based on work by Han et al. After heating 100 mL of DI H₂O to boiling in a round-bottom flask fit with a reflux condenser, 1.06 g of PVP29 was added, followed by 3 mL of 2 M HCl(aq). Once the reaction was refluxing, 0.53 mL of 0.47 M Na₂PdCl₄(aq) was added, and 80 mL of EtOH was poured in slowly. The reaction refluxed for 3 h before being removed from heat.

Incipient Wetness Preparation of Pd/SiO₂ (iw). A 1.78% (w/w) Pd/SiO₂ (iw) catalyst was prepared by incipient wetness impregnation. An aqueous solution of 0.2 g of Pd(NO₃)₂ dissolved in 19.0 mL of DI H₂O was added to 4 g of silica. The resultant material was dried in an oven in air at 40 °C overnight, then calcined under flowing O₂(g) at 300 °C for 2 h, ramping the temperature to the set point at a rate of 5 °C/min.

lon Exchange Preparation of Pd/SiO₂ (ie). A 0.6% (w/w) Pd/SiO₂ sample was prepared by ion exchange (Pd/SiO₂ (ie)). Silica powder was mixed with 50 mL of DI H₂O to form a suspension. Pd ions were added by dropwise addition of a solution of 1.6 g of Pd[(NH₃)₄](NO₃)₂ in 40 mL of DI H₂O. The pH of the solution was 9 and was not adjusted to be otherwise. Afterward, the solvent was removed by filtration, and the catalyst was washed three times with DI H₂O before being dried in an oven at 100 °C overnight. The catalyst was then calcined under flowing O₂(g) with a temperature ramp of 0.5 °C/min from room temperature to 250 °C, where it was held for 2 h.

Catalyst Preparation. Silica-supported nanoparticle catalysts were made by first concentrating each nanoparticle

solution 4-fold by flowing nitrogen over the surface of the stirring solution. Silica was plasma cleaned for an hour prior to being dispersed in solvent and combined with the concentrated nanoparticle solution. The mixture was centrifuged to precipitate out the catalyst as a gel. For the AuPd NP and Au NP catalysts, 0.27 g of plasma-cleaned silica was dispersed in 20 mL of DI H₂O and was centrifuged at 15,000 rpm for 1 h. The precipitated catalyst was washed two times in 15 mL of DI H₂O after this initial centrifugation step at 15,000 rpm for 20 min to remove any unreacted Pd ion or excess PVP55 from the catalyst. Each batch of Pd NPs was mixed with 0.73 g of plasma-cleaned silica dispersed in 80 mL of acetone. This sample was not washed after centrifugation because aggregation of the nanoparticles was observed after a second centrifugation step. After centrifugation, the catalysts were dried under vacuum at 100 °C for 5 h. For each catalyst prepared from a colloidal nanoparticle solution, the number of nanoparticles per liter of solution per gram of silica was kept at a constant value of $1.01 \times 10^{18} \text{ NP/L g}$.

Catalyst Pretreatment. Prior to testing, the catalysts were calcined in a tube furnace at 300 °C for 1 h under an $O_2(g)$ flow of 0.6 L/min. The temperature was increased to 300 °C at a rate of 5 °C/min. These calcination conditions have previously been shown to remove PVP from AuPd catalysts. For samples used in limonene conversion and for TEM analysis, the catalyst was reduced at 300 °C for 1 h in situ under a stream of 100% $H_2(g)$ flowing at 50 sccm. For characterization with DRIFTS, the catalysts were reduced under 30 sccm 10% $H_2(g)$ in $H_2(g)$ for 1 h, and then under 30 sccm 100% $H_2(g)$ for 30 min.

Catalyst Characterization. Bright-field TEM images of each catalyst were acquired with a Tecnai FEI G2 twin microscope at Duke University, and high-resolution HAADF-STEM images were taken using the JEOL 2010F located at Oak Ridge National Laboratory in Oak Ridge, Tennessee, and the FEI Titan STEM at North Carolina State University. DRIFTS spectra were acquired using a Bruker Optics Vertex 70 FT-IR spectrometer equipped with a Harrick Praying Mantis Diffuse Reflection Accessory with a Praying Mantis High Temperature Reaction Chamber in situ reaction cell and OPUS data analysis software. CO chemisorption measurements were made using a Micromeritics ASAP 2020 Surface Area and Porosity Analyzer to determine active surface area on the catalyst. For CO chemisorption experiments, the catalysts were reduced at 300 °C in H₂(g) during analysis. Difference results (total CO – weakly adsorbed CO) are reported. Inductively coupled plasma atomic emission spectroscopy (ICP-AES) analysis was performed by Galbraith Laboratories.

Limonene and Menthane Reactor Conditions. The limonene and menthane conversion reactions were carried out in a homemade vapor phase glass tube reactor coupled to an HP 5890 Series II gas chromatograph. For each run, 250 mg of calcined catalyst was loaded into the reactor, where it was reduced under 50 sccm $H_2(g)$ at 300 °C for 1 h. Immediately after reduction, the reactor temperature was dropped to 250 °C, and α -limonene or p-menthane was continuously injected by syringe pump (Harvard Instruments) at 6 μ L/min. All lines were kept at 220 °C. The GC utilized an FID detector, and the oven temperature was maintained at 80 °C, with He(g) as the carrier gas through a Restek Stabiliwax Bonded Packed Column (Cat# 80416-810). Injections were performed every 10 min. Once the reactor temperature and the feed flow stabilized, the reactor was run between 1.5 and 3 h.

RESULTS AND DISCUSSION

Characterizing the Pd@Au NP Structure. Figure 1 shows high-resolution HAADF-STEM images of the three core—shell

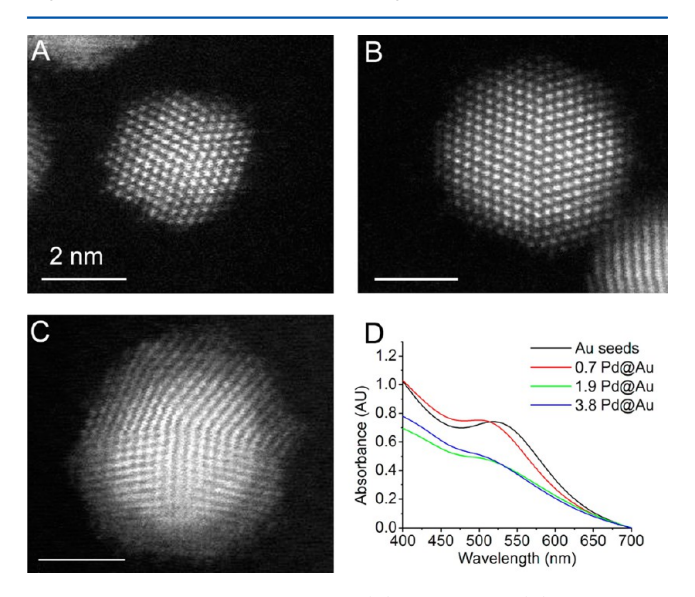


Figure 1. HAADF-STEM images of (A) 0.7 Pd@Au, (B) 1.9 Pd@Au, and (C) 3.8 Pd@Au nanoparticles after synthesis. Panel D shows the UV—visible spectra of the nanoparticles in aqueous solution.

Pd@Au nanoparticles before deposition on the silica support. The HAADF imaging technique provides *z*-contrast, making the Pd shell appear less intense than the Au core. The observed Pd shell thickness corresponds closely with the number of monolayers expected, as calculated from the amount of Na₂PdCl₄(aq) introduced into each Au seed solution, deviating only in the case of the 3.8 Pd@Au particles (see Table S1, Supporting Information). These and other images were used to obtain the shell thicknesses of 0.7, 1.9, and 3.8 atomic monolayers for the core—shell particles. Here, 0.7 indicates an incomplete monolayer. Figure 1D shows that the 520 nm peak characteristic of Au nanoparticles blue shifts and disappears upon the addition of Pd.

TEM size distributions of the Au NPs and the AuPd NPs are shown in Figure 2. The Au seeds are 4.3 \pm 0.6 nm in diameter. The calculated average diameters of the 0.7, 1.9, and 3.8 Pd@ Au particles are 4.6 \pm 0.6, 4.9 \pm 0.6, and 5.2 \pm 0.8 nm, respectively. The relative standard deviation, representing the polydispersity of the particles, is 13.2 \pm 1.3% for all of the particles. The average size of the Au seed was subtracted from the average sizes of the Pd@Au particles to give the average shell thicknesses shown in Figure 2.

After depositing the nanoparticles onto the silica support, the compositions of the catalysts were analyzed by ICP-AES. This data was used to calculate the shell thickness using the density of bulk Pd (12.02 g/cm³) and the Au seed diameter as determined from bright-field TEM. Table S1, Supporting Information, compares these shell thicknesses derived from ICP-AES with those measured by bright-field TEM and HAADF-STEM, while Table S2, Supporting Information, presents the same data in terms of nanoparticle composition. The values determined by ICP-AES match reasonably well with the shell thicknesses (and thus compositions) calculated from the bright-field TEM images. We hypothesize that the difference between the HAADF and the average values from

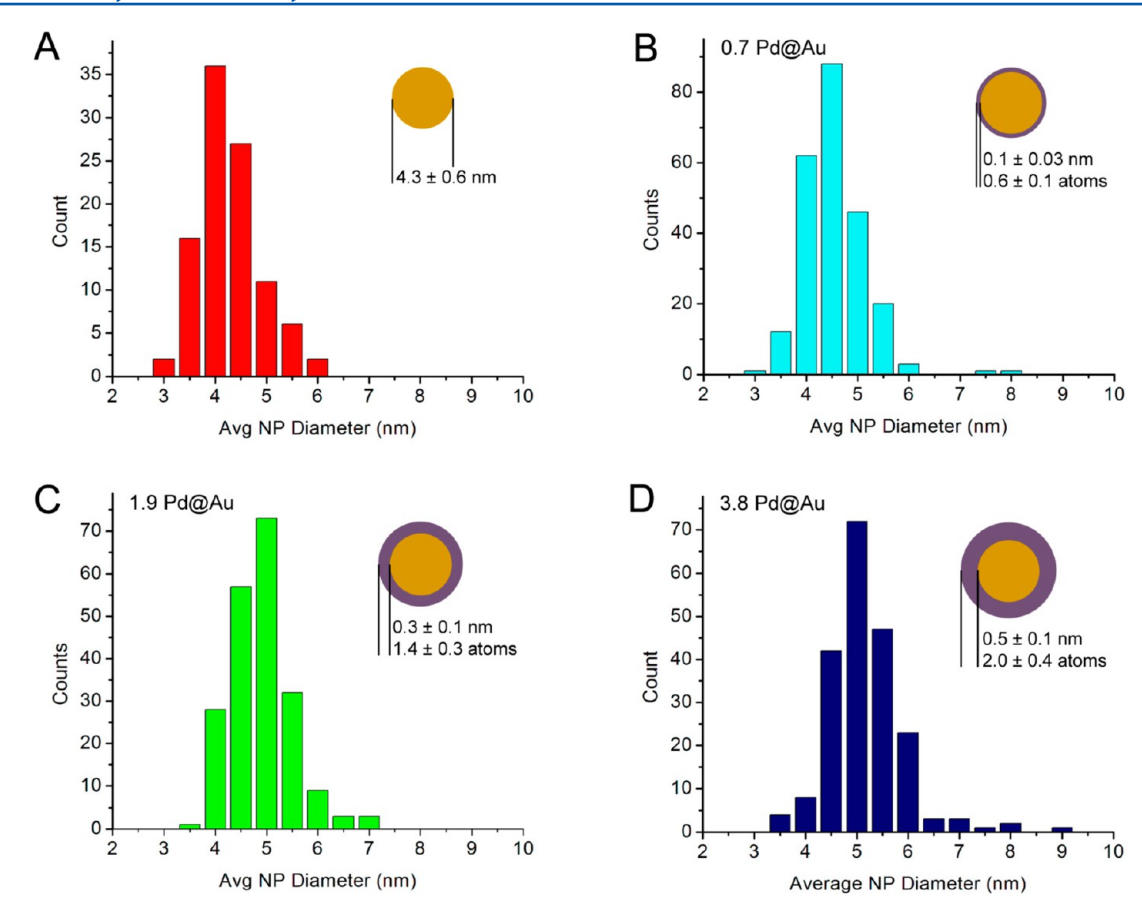


Figure 2. Histograms of the size of Au and AuPd nanoparticles. The relative standard deviation of the particle size is $13.2 \pm 1.3\%$ for all of the particles.

TEM and ICP-AES stems from the fact that the Pd shell becomes more jagged and uneven as it grows in thickness, leading to a shell that appears thicker in HAADF-STEM imaging mode than can be accounted for by comparing the ratio of Pd to Au in the sample. This hypothesis is supported by observations that the intensity of the Pd shell around the 3.8 Pd@Au in Figure 1C is not uniform and that the outer edge of the particle appears to be irregular. Although they contain some error due to the hypothesized jagged nature of the shell, the HAADF-STEM measurements of shell thickness on individual nanoparticles give a sense of the variance in the composition between the nanoparticles. In comparison, the bright-field TEM and ICP-AES measurements can only give a sense of the average composition, with the variance principally coming from the variance in the diameters of the Au seeds.

Effect of Pretreatment on Catalyst Structure. After the nanoparticles were deposited on the SiO₂ support, each catalyst was calcined at 300 °C to remove PVP.²⁰ The catalysts were subsequently heated in flowing H₂(g) at 300 °C to reduce any palladium oxide that was formed. The TEM images in Figure 3 reveal the morphological changes to the Au/SiO₂, the Pd/SiO₂ (PVP), and 3.8 Pd@Au/SiO₂ catalysts after each step in the process. These images show that the monometallic Pd nanoparticles become larger after heat treatment, indicating that they sinter during the process. In contrast, the Au and AuPd particles do not sinter, and their size stays relatively constant after heating. Figure 4 quantifies the effect of pretreatment on the size of the nanoparticles, further illustrating the different sintering behaviors of the AuPd and Pd particles. Figure S1, Supporting Information, shows that the

Pd/SiO₂ (PVP) catalyst agglomerates to form larger particles predominantly during calcination and that the size does not increase much more during reduction.

Previous studies have shown Pd nanoparticles sinter in an oxidative environment at temperatures below 300 °C, presumably due to the formation of PdO, which improves the wetting and migration of Pd across an oxide support.²⁷ In contrast, the propensity of the AuPd nanoparticles to resist sintering under the same conditions appears to be unprecedented in the literature and suggests that the presence of gold prevents the oxidation of Pd. EDX images in Figure 5 show the very clear transition of the 3.8 Pd@Au nanoparticles from a core-shell structure to a homogeneous alloy after calcination. This observation is a second piece of evidence that the presence of gold prevents the formation of PdO in these nanoparticles, as PdO does not alloy with Au. Previous electrochemical experiments have also shown that thin layers of palladium deposited on a gold electrode oxidized at a higher applied potential than pure palladium.²⁹ Auger electron and photoelectron spectroscopic analysis of AuPd alloyed surfaces have revealed that when the alloy surface is Au-rich, it does not oxidize in the presence of oxygen between 300 and 600 °C. 30 Conversely, Pd-rich surfaces are coated with a layer of PdO under similar conditions.³¹ We hypothesize that, in the Au-rich AuPd system described here, Au inhibits PdO generation under oxidizing conditions, which in turn prevents sintering.

DRIFT spectra of adsorbed CO on the catalysts before and after calcination/reduction provide further evidence that the Pd@Au nanoparticles undergo alloying during pretreatment. CO DRIFT spectra of the as-prepared catalysts after in situ

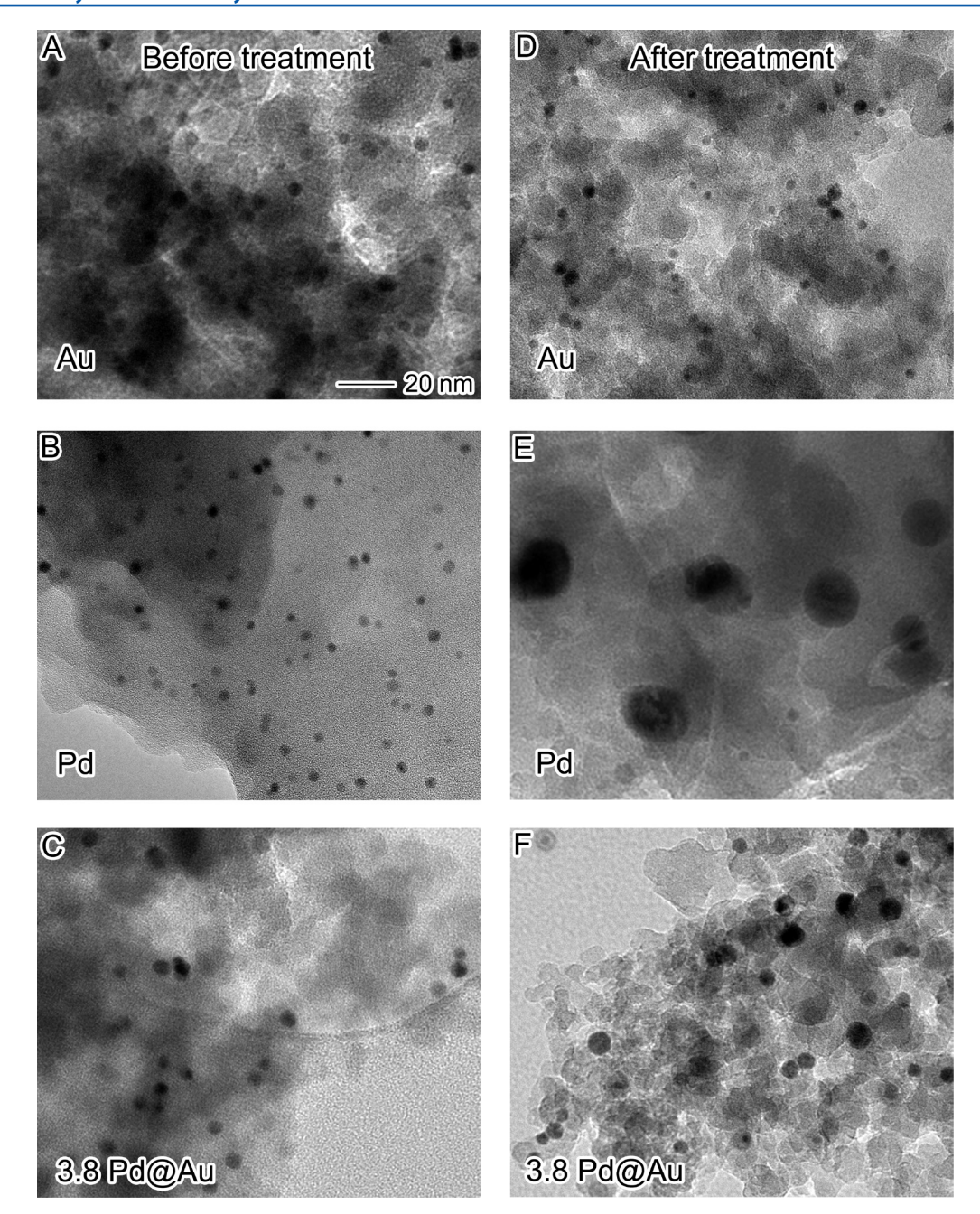


Figure 3. TEM images of Au/SiO2, Pd/SiO2, and 3.8 Pd@Au/SiO2 before and after calcination and reduction at 300 °C.

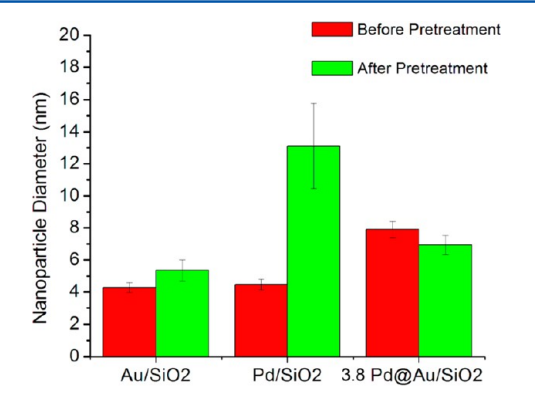


Figure 4. Average diameters of nanoparticles before and after calcination and reduction at 300 $^{\circ}\mathrm{C}.$

treatment in flowing $H_2(g)$ at 25 °C (to reduce any superficial PdO_x) are shown in Figure 6A. The observed CO stretching frequencies (2032 and 1932 cm⁻¹) are assigned to linear (atop) CO and 2-fold bridging CO on Pd, respectively, in agreement with similar frequency assignments for adsorbed CO on various Pd model catalysts.^{31–38} The relative intensity of the very strong bridging CO band increases with nominal Pd shell thickness, indicating a higher density of multiatom Pd surface ensembles at higher Pd loadings. The DRIFT spectrum of adsorbed CO on the Pd/SiO₂ (iw) catalyst, shown in Figure S2A, Supporting Information, exhibits analogous bands at 2094 and 1990 cm⁻¹ that can be assigned to atop and bridging CO; however, they are shifted \sim 60 cm⁻¹ to higher wavenumbers relative to those observed for the Pd@Au catalysts (Figure 6A). At saturation coverage, peaks in the 1970–1990 cm⁻¹ region have been assigned to doubly bridging CO on Pd(100) facets

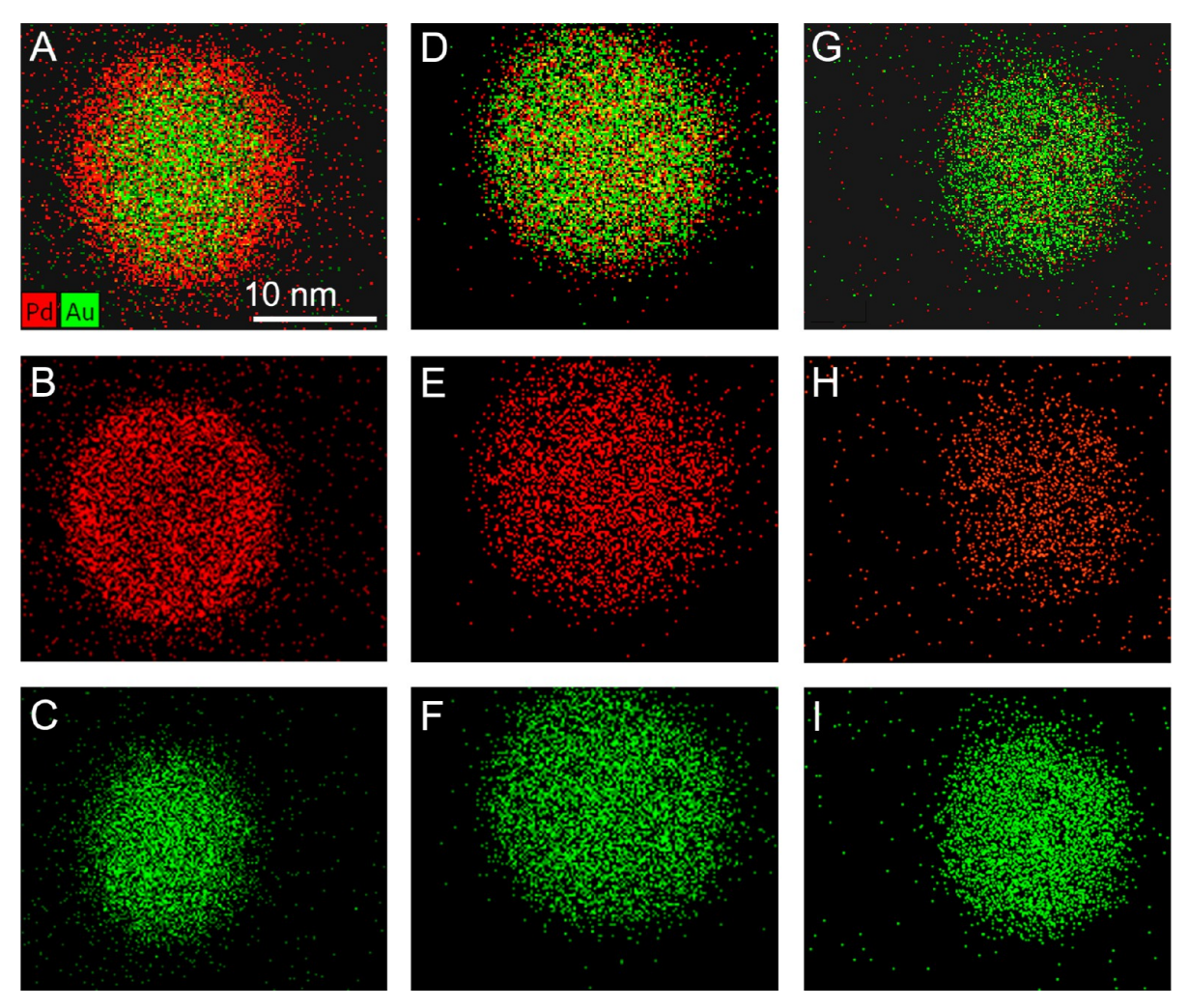


Figure 5. EDX-STEM images of 3.8 Pd@Au (A-C) before pretreatment, (D-F) after calcination at 300 $^{\circ}$ C, and (G-I) after calcination and reduction at 300 $^{\circ}$ C.

and at particle steps and edges.³² The Pd/SiO₂ (iw) catalyst contains faceted 4-5 nm Pd nanoparticles (Figure S2B, Supporting Information) that are closely similar in size to the supported Pd@Au core-shell nanoparticles. The decrease (red shift) in CO stretching frequencies observed when Au is present in the core of the particle suggests that Au donates d electron density to the Pd shell in the Pd@Au configuration. This provides a viable explanation for why Au inhibits the oxidation of Pd during the calcination step, in that Au moves the Pd d band center away from the Fermi level and weakens its interaction with adsorbed species, including oxygen.³ The CO DRIFT spectra in Figure 6B were recorded after in situ treatment in flowing H₂(g) at 100 °C. The spectra are qualitatively similar to those in Figure 6A, indicating retention of a core-shell structure after heating under hydrogen at 100 °C. In this case, the intensities of the CO stretching peaks at 1932 cm⁻¹ for the 1.9 and 3.8 Pd@Au/SiO₂ catalysts are comparable. We note that, as with previous CO DRIFTS studies, the presence of PVP on the particles in Figure 6A,B did not prevent the adsorption of CO.35

There are three significant changes in the CO DRIFT spectra after calcination and reduction of the $Pd@Au/SiO_2$ catalysts (Figure 6C). First, a linear Au–CO stretch at 2100 cm⁻¹ appears in each of the spectra. This indicates that Au atoms have migrated to the surface of the particles. This

conclusion is reinforced by the observation that the intensity of the linear Pd-CO stretch relative to the 2-fold Pd-CO bridging stretch is larger in all cases, indicating the break-up of multiatom Pd ensembles. There is also a 28 cm⁻¹ blue shift of the Pd-CO linear and 2-fold stretches to 2060 and 1960 cm⁻¹ respectively. The blue shift of these CO stretching frequencies may indicate that a subtle shift of d electron density from Pd to Au occurs upon conversion from a core-shell to an alloy structure; however, this shift may also be due to variations in dipole—dipole coupling that can also affect CO stretching frequencies.^{3,33} The CO frequencies remain red-shifted from the typical linear and 2-fold bridging CO stretches observed for Pd/SiO₂ (iw) (2090 and 1990 cm⁻¹, respectively), implying that there is electron transfer from Au to the Pd d band in both the core-shell and alloy structures. 33,37 We note the small shoulder at 2050 cm⁻¹ that closely matches a shoulder assigned by Marx et al. as a linear Au-CO species on AuPd alloy nanoparticles and tentatively assign this shoulder as CO bound to surface Au on the AuPd alloy catalysts investigated in this study.33

Selectivity of AuPd Nanoparticles in Limonene Conversion. The reaction data in Figure 7A demonstrate that the solution-synthesized catalysts were active for the conversion of limonene to *p*-cymene. The yield of *p*-cymene was 65.5%, 83.2%, and 84.1% over the 10.9%, 20%, and 28.5%

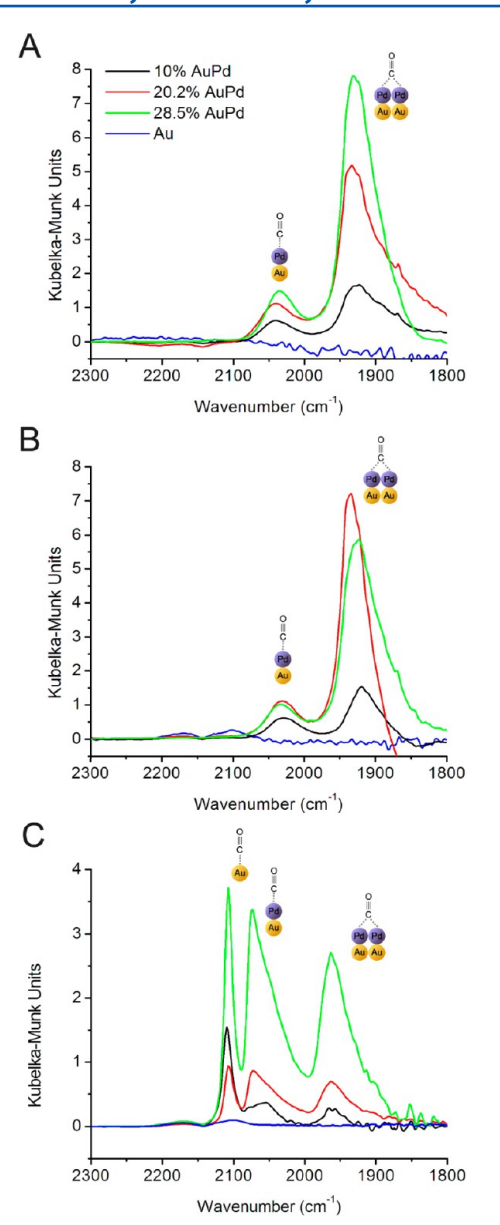


Figure 6. DRIFT spectra of adsorbed CO on supported Pd@Au/SiO $_2$ catalysts (A) after heating in flowing $H_2(g)$ at 25 °C, (B) after heating in flowing $H_2(g)$ at 100 °C, and (C) after calcination and reduction at 300 °C.

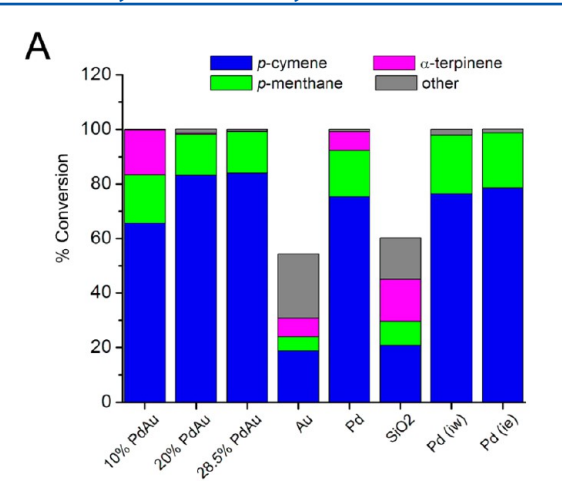
AuPd catalysts, respectively, with 100% conversion of limonene. The conversion of limonene over the Au/SiO2 catalyst and silica control was 54% and 60%, respectively. Only 18.6% of the limonene was converted to p-cymene over the Au/SiO₂ catalyst, and a significant portion of the rest of the product stream comprised unidentified products. The Pd/SiO₂ catalysts all performed similarly to one another, fully converting limonene and yielding approximately 80% p-cymene. In addition to ρ -cymene, the Pd nanoparticle catalyst yielded α terpinene and ρ -menthane, while the Pd catalysts prepared by incipient wetness and ion exchange yielded only p-menthane. The 10% AuPd catalyst yielded α -terpinene as well, but the 20% and 28.5% AuPd catalysts did not. Figure 7B shows the Au/SiO₂ catalyst and silica readily deactivated, whereas the productivity of the Pd-containing catalysts was relatively constant with time on stream.

Previous work suggests that α -limonene conversion to pcymene over silica-supported Pd catalysts proceeds via a twostep hydrogenation/dehydrogenation pathway, in which pmenthane is an intermediate and isomers are produced as byproducts only in the absence of Pd or $H_2(g)$. However, our results suggest that silica-supported Pd and AuPd catalysts produce p-cymene by an isomerization-dehydrogenation pathway, similar to that reported for solution-phase Pd nanoparticles.²² We base this conclusion on the very low vield of p-cymene produced over each catalyst when pmenthane was employed as the reactant at 250 °C (Table 1). This result is surprising given that p-cymene is the thermodynamically favored product at this temperature.²² If p-cymene were primarily produced via reversible dehydrogenation of p-menthane, one would expect to see a pattern in the turnover frequencies (TOFs) of the catalysts that is similar to the yields of p-cymene in Figure 7A. However, there is no correspondence between the TOFs shown in Table 1 and the selectivity toward p-cymene in Figure 7A. Given these results, we propose Scheme 1 as the pathway of conversion from limonene to p-cymene, with p-menthane being formed as a byproduct rather than an intermediate in the production of pcymene.

Finally, we note that the 10% AuPd catalyst has the highest turnover frequency (TOF) for p-menthane dehydrogenation. All of the other supported Pd catalysts have p-menthane TOFs in the $\sim 10-20~h^{-1}$ range. It has previously been observed that small islands of Pd deposited on Au surfaces evolve hydrogen at higher rates than a Pd surface. This enhancement could be attributed to surface diffusion of atomic hydrogen from Pd sites to the surrounding inert Au atoms, which makes it easier for hydrogen to associatively desorb from the catalyst surface. An analogous effect might be responsible for the higher activity of the 10% AuPd surface for p-menthane dehydrogenation. The other two AuPd/SiO $_2$ catalysts have TOFs of 20 h $^{-1}$, similar to the value for the highly dispersed Pd/SiO $_2$ (ie), suggesting a possible ensemble-size effect.

CONCLUSIONS

We report the synthesis of monodisperse, well-defined Au nanoparticles with Pd shells of varying thickness in a catalytically relevant size range (\le 5 nm). These core-shell particles were deposited on SiO₂, calcined to remove PVP, and reduced to obtain a set of alloy AuPd nanoparticle catalysts with three different Pd contents. Examination of changes in particle size by TEM and changes in morphology by EDX before and after calcination under oxygen at 300 °C indicate the addition of Au to a Pd nanoparticle can prevent its oxidation and thus prevent its migration and sintering on an oxide support. CO DRIFTS confirmed the diffusion of Au to the surface of the particles after oxidation and reduction at 300 °C, and the transfer of electron density from Au to Pd. The AuPd alloy catalysts were active for the conversion of limonene to p-cymene; the particles containing greater than 20% Pd exhibited p-cymene yields (~80%) approximately equivalent to that observed for the Pd catalysts prepared by incipient wetness and ion exchange. The AuPd catalyst with the lowest Pd content (10.9%) exhibited a TOF for p-menthane dehydrogenation about an order of magnitude greater than catalysts with higher Pd contents. The catalytic results presented here suggest p-cymene is formed through the formation of an α -terpinene intermediate rather than through the dehydrogenation of pmenthane.



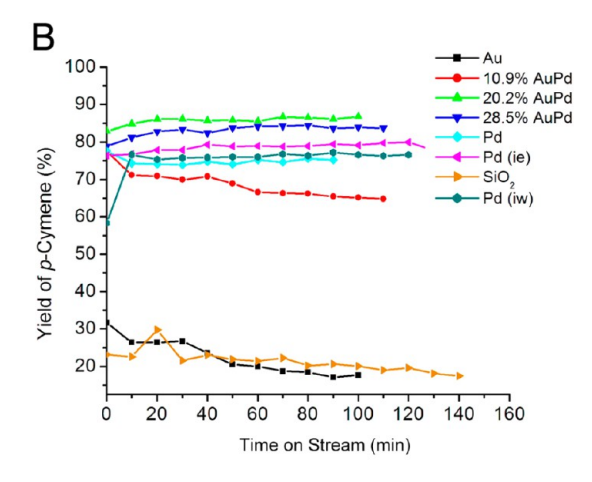


Figure 7. (A) Percent conversion of α-limonene to p-cymene, p-menthane, α-terpinene, and other unidentified products over each catalyst and the silica support. The full height of each bar signifies the percent conversion of limonene, while the height of each product represents the percent yield. (B) The yield of p-cymene as a function of time on stream for each catalyst at 250 °C.

Table 1. CO Adsorbed (μ mol/g) of Total Catalyst (Metal and Silica Support); p-Menthane Conversion Refers to the Percentage of Menthane Dyhydrogenated to Form p-Cymene; TOF Refers to the mol/h of p-Menthane Converted to p-Cymene per mol CO Adsorbed; p-Menthane Feed Rate Was 6 μ L/min, the Reaction Temperature Was 250 °C, and the Catalyst Mass for Each Run Was 0.250 g

catalyst	CO adsorbed $(\mu \text{mol/g})$	<i>p</i> -menthane conversion (%)	TOF (h^{-1})
10% AuPd	0.69 ± 0.1	1.42 ± 0.008	162.7 ± 17.8
20% AuPd	5.13 ± 0.6	1.39 ± 0.001	20.8 ± 2.4
28.5% AuPd	5.51 ± 0.7	1.32 ± 0.06	16.1 ± 2.0
Pd/SiO ₂	0.77 ± 0.2	1.23 ± 0.001	7.6 ± 0.09
Pd/SiO ₂ (ie)	27.1 ± 1.4	7.17 ± 0.2	21.3 ± 0.8
Pd/SiO ₂ (iw)	15.7 ± 0.8	1.88 ± 0.09	9.7 ± 0.3

Scheme 1. Proposed Scheme of Limonene Conversion to p-Cymene and p-Menthane

Going forward, we would ideally like to compare the catalytic properties of the core—shell AuPd particles with the properties of the alloys to gain further insights into the relative contributions of ensemble, ligand, and spillover effects to a catalyst's activity and selectivity. 40 However, for AuPd nanoparticles in a catalytically relevant size range, we show that such an analysis can only be performed for relatively lowtemperature reactions; otherwise, the core-shell nanoparticles will alloy. Elimination of the need to burn off PVP at 300 °C is a secondary prerequisite to comparing the properties of the core-shell and alloyed nanoparticles. Although the AuPd synthesis did not require the use of PVP, we found PVP to be helpful in dispersing the nanoparticles evenly across the SiO₂ and prevent their aggregation during drying. Thus, an improved method for depositing the nanoparticles on a support would eliminate the need for PVP. Although obstacles remain, this work represents an important step toward understanding how to prepare and characterize model nanoparticle catalysts for testing mechanistic hypotheses. In particular, the quantification of the per particle variance in composition by simply measuring changes in size may facilitate the preparation and comparison of catalysts that are not only monodisperse in size but also in composition.

ASSOCIATED CONTENT

S Supporting Information

Comparison of the Pd shell thicknesses calculated using ICP-AES, bright-field TEM, and HAADF-STEM measurements; bright-field TEM images of the Pd/SiO₂ (PVP) before pretreatment, after calcination, and after calcination and subsequent reduction; and the DRIFT spectrum and a HAADF-STEM image of the Pd/SiO₂ catalyst prepared by incipient wetness impregnation. This material is available free of charge via the Internet at http://pubs.acs.org.

AUTHOR INFORMATION

Corresponding Author

*E-mail: benjamin.wiley@duke.edu (B.J.W.); lamb@ncsu.edu (H.H.L.).

Notes

The authors declare no competing financial interest.

ACKNOWLEDGMENTS

We acknowledge support from the NSF EFRI HyBi grant (EFRI-0937721), start-up funds from Duke University, and ORNL's Share User Facility, which is sponsored by the

Scientific User Facilities Division, Office of Basic Energy Sciences, U.S. Department of Energy. A.R.W. is supported through the National Science Foundation Graduate Research Fellow Program. This work made use of the Analytical Instrumentation Facility at NCSU.

REFERENCES

- (1) Coq, B.; Figueras, F. Bimetallic Palladium Catalysts: Influence of the Co-Metal on the Catalyst Performance. *J. Mol. Catal. A: Chem.* **2001**, *173*, 117–134.
- (2) Ferrer, D.; Torres-Castro, A.; Gao, X.; Sepúlveda-Guzmán, S.; Ortiz-Méndez, U.; José-Yacamán, M. Three-Layer Core/Shell Structure in Au-Pd Bimetallic Nanoparticles. *Nano Lett.* **2007**, *7*, 1701–1705.
- (3) Gao, F.; Goodman, D. W. Pd-Au Bimetallic Catalysts: Understanding Alloy Effects from Planar Models and (Supported) Nanoparticles. *Chem. Soc. Rev.* **2012**, *41*, 8009–8020.
- (4) Enache, D. I.; Edwards, J. K.; Landon, P.; Solsona-Espriu, B.; Carley, A. F.; Herzing, A. A.; Watanabe, M.; Kiely, C. J.; Knight, D. W.; Hutchings, G. J. Solvent-Free Oxidation of Primary Alcohols to Aldehydes Using Au–Pd/TiO₂ Catalysts. *Science* **2006**, *311*, 362–365.
- (5) Chen, Y.; Lim, H.; Tang, Q.; Gao, Y.; Sun, T.; Yan, Q.; Yang, Y. Solvent-Free Aerobic Oxidation of Benzyl Alcohol over Pd Monometallic and Au–Pd Bimetallic Catalysts Supported on SBA-16 Mesoporous Molecular Sieves. *Appl. Catal.*, A 2010, 380, 55–65.
- (6) Ham, H. C.; Hwang, G. S.; Han, J.; Nam, S. W.; Lim, T. H. Geometric Parameter Effects on Ensemble Contributions to Catalysis: H₂O₂ Formation from H₂ and O₂ on AuPd Alloys. A First Principles Study. *J. Phys. Chem. C* **2010**, *114*, 14922–14928.
- (7) Liu, P.; Norskov, J. K. Ligand and Ensemble Effects in Adsorption on Alloy Surfaces. *Phys. Chem. Chem. Phys.* **2001**, 3, 3814–3818.
- (8) Kumar, D.; Chen, M. S.; Goodman, D. W. Synthesis of Vinyl Acetate on Pd-Based Catalysts. *Catal. Today* **2007**, *123*, 77–85.
- (9) Rebelli, J.; Detwiler, M.; Ma, S.; Williams, C. T.; Monnier, J. R. Synthesis and Characterization of Au–Pd/SiO₂ Bimetallic Catalysts Prepared by Electroless Deposition. *J. Catal.* **2010**, *270*, 224–233.
- (10) Meenakshisundaram, S.; Nowicka, E.; Miedziak, P. J.; Brett, G. L.; Jenkins, R. L.; Dimitratos, N.; Taylor, S. H.; Knight, D. W.; Bethell, D.; Hutchings, G. J. Oxidation of Alcohols Using Supported Gold and Gold-Palladium Nanoparticles. *Faraday Discuss.* **2010**, *145*, 341–356.
- (11) Solsona, B. E.; Edwards, J. K.; Landon, P.; Carley, A. F.; Herzing, A.; Kiely, C. J.; Hutchings, G. J. Direct Synthesis of Hydrogen Peroxide from H₂ and O₂ Using Al₂O₃ Supported Au–Pd Catalysts. *Chem. Mater.* **2006**, *18*, 2689–2695.
- (12) Chai, J.; Li, F.; Hu, Y.; Zhang, Q.; Han, D.; Niu, L. Hollow Flower-Like AuPd Alloy Nanoparticles: One Step Synthesis, Self-Assembly on Ionic Liquid-Functionalized Graphene, and Electro-oxidation of Formic Acid. *J. Mater. Chem.* **2011**, 21, 17922–17929.
- (13) Pawelec, B.; Venezia, A. M.; La Parola, V.; Cano-Serrano, E.; Campos-Martin, J. M.; Fierro, J. L. G. AuPd Alloy Formation in Au–Pd/Al₂O₃ Catalysts and Its Role on Aromatics Hydrogenation. *Appl. Surf. Sci.* **2005**, *242*, 380–391.
- (14) Venezia, A. M.; Parola, V. L.; Pawelec, B.; Fierro, J. L. G. Hydrogenation of Aromatics over Au–Pd/SiO₂–Al₂O₃ Catalysts; Support Acidity Effect. *Appl. Catal., A* **2004**, *264*, 43–51.
- (15) Baber, A. E.; Tierney, H. L.; Sykes, E. C. H. Atomic-Scale Geometry and Electronic Structure of Catalytically Important Pd/Au Alloys. ACS Nano 2010, 4, 1637–1645.
- (16) Ketchie, W. C.; Murayama, M.; Davis, R. J. Selective Oxidation of Glycerol over Carbon-Supported AuPd Catalysts. *J. Catal.* **2007**, 250, 264–273.
- (17) Guczi, L.; Beck, A.; Horváth, A.; Koppány, Z.; Stefler, G.; Frey, K.; Sajó, I.; Geszti, O.; Bazin, D.; Lynch, J. AuPd Bimetallic Nanoparticles on TiO₂: XRD, TEM, in Situ EXAFS Studies and Catalytic Activity in CO Oxidation. *J. Mol. Catal. A: Chem.* **2003**, 204–205, 545–552.

- (18) Xu, J.; Wilson, A. R.; Rathmell, A. R.; Howe, J.; Chi, M.; Wiley, B. J. Synthesis and Catalytic Properties of Au–Pd Nanoflowers. *ACS Nano* **2011**, *5*, 6119–6127.
- (19) Zhou, W.; Lee, J. Y. Highly Active Core—Shell Au@Pd Catalyst for Formic Acid Electrooxidation. *Electrochem. Commun.* **2007**, *9*, 1725—1729.
- (20) Dash, P.; Bond, T.; Fowler, C.; Hou, W.; Coombs, N.; Scott, R. W. J. Rational Design of Supported PdAu Nanoparticle Catalysts from Structured Nanoparticle Precursors. *J. Phys. Chem. C* **2009**, *113*, 12719–12730.
- (21) Corma, A.; Iborra, S.; Velty, A. Chemical Routes for the Transformation of Biomass into Chemicals. *Chem. Rev.* **2007**, *107*, 2411–2502.
- (22) Zhao, C.; Gan, W.; Fan, X.; Cai, Z.; Dyson, P. J.; Kou, Y. Aqueous-Phase Biphasic Dehydroaromatization of Bio-Derived Limonene into *p*-Cymene by Soluble Pd Nanocluster Catalysts. *J. Catal.* **2008**, 254, 244–250.
- (23) Reddy, K. S. N.; Rao, B. S.; Shiralkar, V. P. Selective Formation of Cymenes over Large Pore Zeolites. *Appl. Catal., A* **1995**, *121*, 191–201
- (24) Harvey, B. G.; Wright, M. E.; Quintana, R. L. High-Density Renewable Fuels Based on the Selective Dimerization of Pinenes. *Energy Fuels* **2009**, *24*, 267–273.
- (25) Buhl, D.; Roberge, D. M.; Hölderich, W. F. Production of p-Cymene from α -Limonene over Silica Supported Pd Catalysts. *Appl. Catal.*, A 1999, 188, 287–299.
- (26) Han, J.; Sun, H.; Duan, J.; Ding, Y.; Lou, H.; Zheng, X. Palladium-Catalyzed Transformation of Renewable Oils into Diesel Components. *Adv. Synth. Catal.* **2010**, *352*, 1805–1809.
- (27) Gabasch, H.; Unterberger, W.; Hayek, K.; Klötzer, B.; Kleimenov, E.; Teschner, D.; Zafeiratos, S.; Hävecker, M.; Knop-Gericke, A.; Schlögl, R.; Han, J.; Ribeiro, F. H.; Aszalos-Kiss, B.; Curtin, T.; Zemlyanov, D. In Situ XPS Study of Pd(111) Oxidation at Elevated Pressure, Part 2: Palladium Oxidation in the 101 mbar Range. Surf. Sci. 2006, 600, 2980–2989.
- (28) Chen, J. J.; Ruckenstein, E. Role of Interfacial Phenomena in the Behavior of Alumina-Supported Palladium Crystallites in Oxygen. *J. Phys. Chem.* **1981**, *85*, 1606–1612.
- (29) Moss, R. L.; Pope, D.; Davis, B. J.; Edwards, D. H. The Structure and Activity of Supported Metal Catalysts: VIII. Chemisorption and Benzene Hydrogenation on Palladium/Silica Catalysts. *J. Catal.* **1979**, 58, 206–219.
- (30) Cadle, S. H. Electrochemical Oxidation of Thin Palladium Films on Gold. *Anal. Chem.* **1974**, *46*, 587–590.
- (31) Hilaire, L.; Légaré, P.; Holl, Y.; Maire, G. Interaction of Oxygen and Hydrogen with Pd–Au Alloys: An AES and XPS Study. *Surf. Sci.* **1981**, *103*, 125–140.
- (32) Lear, T.; Marshall, R.; Lopez-Sanchez, J. A.; Jackson, S. D.; Klapotke, T. M.; Baumer, M.; Rupprechter, G.; Freund, H.-J.; Lennon, D. The Application of Infrared Spectroscopy to Probe the Surface Morphology of Alumina-Supported Palladium Catalysts. *J. Chem. Phys.* **2005**, *123*, 174706.
- (33) Marx, S.; Krumeich, F.; Baiker, A. Surface Properties of Supported, Colloid-Derived Gold/Palladium Mono- and Bimetallic Nanoparticles. *J. Phys. Chem. C* **2011**, *115*, 8195–8205.
- (34) Dellwig, T.; Rupprechter, G.; Unterhalt, H.; Freund, H. J. Bridging the Pressure and Materials Gaps: High Pressure Sum Frequency Generation Study on Supported Pd Nanoparticles. *Phys. Rev. Lett.* **2000**, *85*, 776–779.
- (35) Groppo, E.; Bertarione, S.; Rotunno, F.; Agostini, G.; Scarano, D.; Pellegrini, R.; Leofanti, G.; Zecchina, A.; Lamberti, C. Role of the Support in Determining the Vibrational Properties of Carbonyls Formed on Pd Supported on SiO₂, Al₂O₃, Al₂O₃, and MgO. *J. Phys. Chem. C* **2007**, *111*, 7021–7028.
- (36) Ozensoy, E.; Wayne Goodman, D. Vibrational Spectroscopic Studies on CO Adsorption, NO Adsorption CO + NO Reaction on Pd Model Catalysts. *Phys. Chem. Chem. Phys.* **2004**, *6*, 3765–3778.

- (37) Kelly, M. J.; Kim, J.; Roberts, G. W.; Lamb, H. H. Characterization of Pd/γ -Al₂O₃ Catalysts Prepared Using $[Pd(hfac)_2]$ in Liquid CO₂. *Top. Catal.* **2008**, *49*, 178–186.
- (38) Xu, X.; Goodman, D. W. An Infrared and Kinetic Study of Carbon Monoxide Oxidation on Model Silica-Supported Palladium Catalysts from 10–9 to 15 Torr. *J. Phys. Chem.* **1993**, *97*, 7711–7718.
- (39) Borodko, Y.; Lee, H. S.; Joo, S. H.; Zhang, Y.; Somorjai, G. Spectroscopic Study of the Thermal Degradation of PVP-Capped Rh and Pt Nanoparticles in H_2 and O_2 Environments. J. Phys. Chem. C **2009**, 114, 1117–1126.
- (40) Santana, J. A.; Rosch, N. Hydrogen Adsorption on and Spillover from Au- and Cu-Supported Pt₃ and Pd₃ Clusters: a Density Functional Study. *Phys. Chem. Chem. Phys.* **2012**, *14*, 16062–16069.